
A KOOPMAN APPROACH TO UNDERSTANDING SEQUENCE NEURAL MODELS

A PREPRINT

Ilan Naiman

Department of Computer Science
Ben-Gurion University
naimani@post.bgu.ac.il

Omri Azencot

Department of Computer Science
Ben-Gurion University
azencot@cs.bgu.ac.il

ABSTRACT

We introduce a new approach to understanding trained sequence neural models: the Koopman Analysis of Neural Networks (KANN) method. Motivated by the relation between time-series models and self-maps, we compute approximate *Koopman operators* which encode well the latent dynamics. Unlike other existing methods whose applicability is limited, our framework is global, and it has only weak constraints over the inputs. Moreover, the Koopman operator is linear, and it is related to a rich mathematical theory. Thus, we can use tools and insights from linear analysis and Koopman Theory in our study. For instance, we show that the operator eigendecomposition is instrumental in exploring the dominant features of the network. Our results extend across tasks and architectures as we demonstrate for the copy problem, and ECG classification and sentiment analysis tasks.

Keywords Koopman theory, Sequence models

1 Introduction

Understanding the inner workings of predictive models is an essential requirement in many disciplines across science and engineering. This requirement is even more important nowadays with the emergence of neural networks whose visualization and interpretation is inherently challenging. Indeed, modern computational neural models often lack a commonly accepted knowledge regarding their governing mathematical principles. Consequently, while deep neural networks may achieve groundbreaking results on various complex tasks, explaining their underlying decision mechanisms remains a challenge. The goal of this paper is to help bridge this gap by proposing a new framework for the approximation, reasoning, and understanding of sequence neural models.

Sequence models are designed to handle time-series data originating from images, text, audio, and other sources of information. One approach to analyzing sequence neural networks is through the theory and practice of dynamical systems [1, 2]. For instance, the temporal asymptotic behavior of a dynamical system can be described using the local analysis of its attractor states [3]. Similarly, recurrent models have been investigated in the neighborhood of their fixed points [4], leading to works that interpret trained RNNs for tasks such as sentiment analysis [5] and text classification [6]. However, the local nature of these methods may result in failure cases as we show on the copy task.

Our approach to explaining the underlying mechanisms of trained sequence neural models is motivated by the analogy between RNNs and *self-maps*, i.e., transformations from the domain to itself. Self-maps are extensively studied in differential geometry and dynamical systems, which allows us to facilitate insights and tools from these fields in our setting. Specifically, our method is mainly based on a novel observation of Koopman [7] for representing nonlinear dynamical systems using *linear* objects. Namely, under a mild set of assumptions, the dominant features of general dynamical systems can be captured via a single matrix per system. We call these matrices (approximated) *Koopman operators*, and we use them to reason about neural nets.

Methods based on Koopman’s theory are widely used in the nonlinear dynamics [8, 9] and geometry processing [10, 11] communities. There are several advantages to using Koopman operators in the context of neural networks. First, analyzing matrices is simpler than processing nonlinear representations since linear algebra tools e.g., the eigendecomposition of a matrix, can be used. Second, the dominant modes of the dynamics and their growth and decay are directly related to the eigenvalues and eigenvectors of the Koopman operator. Third, unlike local Jacobian estimates

in the vicinity of a fixed point, the Koopman operator is a *global* encoding, and thus it is virtually applicable to any point. Finally, and most importantly, Koopman-based methods are associated with rich theory and practice, motivating others to further generalize and explore current approaches.

Given a trained sequence neural network and a procedure to extract its hidden states, we generate a moderate size matrix which encodes the dominant features of the latent dynamics. Our approach is simple, yet it provides several instrumental tools for understanding the network. We will show that our technique yields good accuracy results on the copy task using a minimal amount of input. Moreover, on the sentiment analysis task, our framework can reproduce the model behavior using only three vectors and a 3×3 matrix. Further, we will demonstrate in the context of ECG classification task that there is a spectral basis for encoding the hidden states in which the dynamics are fully separable. Given the versatility of our framework and its ease of use, we advocate in what follows the usefulness of our method for the analysis and processing of time-series models.

2 Related Work

RNN and DS. Fully connected recurrent neural networks are universal approximators of arbitrary dynamical systems [12]. Unfortunately, RNNs are well-known to be difficult to train [13, 2], and several methods adopt a DS perspective to improve training via gradient clipping [2], gating [14], and constraining the weights [15], among other approaches. In the same context, avoiding gradient explosion was recently achieved by regularizing the hidden state space via quasi-isometric hidden-to-hidden maps [16, 17]. Overall, it is clear that dynamical systems are fundamental in investigating and developing recurrent networks.

Understanding RNN. Establishing a deeper understanding of recurrent networks is a long standing challenge in machine learning. To do this end, [18, 19] follow the outputs of the model to identify units which track brackets, line lengths, and quotes. An alternative line of work designs quantitative measures to rank the importance of individual inputs to the network outcome [20, 21, 22]. Perhaps mostly related to our approach is the analysis and study of recurrent models around their fixed points [4]. This method revealed low-dimensional attractors in tasks such as sentiment analysis [5] and text classification [6], which allowed to deduce simple explanations of the decision mechanisms of the associated models. Our work generalizes the approach of Sussillo and colleagues [4] in that it yields global results about the dynamics, and it introduces several novel features. We provide a more detailed comparison between our method and theirs in Sec. 4.

Koopman-based Neural Networks. Recently, several techniques that combine neural networks and Koopman theory were proposed, mostly in the context of *predicting* nonlinear dynamics. For example, [23, 24] optimize the residual sum of squares of the predictions the operator makes, [25, 26, 8] design dynamic autoencoders whose central component is linear and may be structured, [27] employ graph networks, and [28] use a variational approach on Markov processes. A recent line of work aims at exploiting tools from Koopman theory to analyze and improve the training process of neural networks [29, 30]. To the best of our knowledge, our work is first to employ a Koopman-based method towards the analysis and understanding of trained neural networks.

3 Method

In what follows, we present our method for analyzing and understanding sequence neural models. Importantly, while we mostly discuss on and experiment with recurrent neural networks, our approach is quite general and applicable to any model whose inner representation is a time-series. We focus on the practical setting in this section, and we provide theoretical justifications for our approach in App. A.

We consider neural models that take the following form

$$h_t = F(h_{t-1}, x_t), \quad t = 1, 2, \dots, \quad (1)$$

where $x_t \in \mathbb{R}^m$ denotes the input instance at time t , h_t is a (hidden) state that represents the dynamical path, and F is some nonlinear function that pushes states through time. From a dynamical systems point-of-view, Eq. (1) may be thought of as an autonomous system that includes control. However, we will also allow an empty control variable x_t in general. All recurrent models including vanilla RNN [31], LSTM [32], and GRU [33], as well as Echo State Networks [34], and Residual neural networks [35] exhibit the structure of Eq. (1).

To study the properties and behavior of F , we propose to generate a linear matrix $C \in \mathbb{R}^{k \times k}$ such that it captures the dominant features of the dynamics. Indeed, F is typically high dimensional and highly nonlinear, and thus it would be a futile attempt to represent an arbitrary F in full via a linear object. Instead, we aim at designing a linear map

Algorithm 1 Koopman Operators using a singular value decomposition and a least-squares minimization

```

1: Input: a set of states  $\{h_{s,t}\}$  extracted from Eq. (1)
2: Output: a matrix  $C \in \mathbb{R}^{k \times k}$  satisfying Eq. (3)
3:  $B := (b_j) = \text{SVD}(\{h_{s,t}\})$ 
4: for  $s, t, j$  do
5:    $\tilde{h}_{s,t}(j) = b_j^T \cdot h_{s,t}$ 
6: end for
7: Solve  $\sum_{s,t,j} [(C\tilde{h}_{s,t})(j) - \tilde{h}_{s,t+1}(j)]^2 = 0$ 
8: Return  $C$ 

```

that holds the potential to describe the dynamics well. In practice, there are several examples of nonlinear dynamical systems which exhibit good approximations using methods that are similar to ours. Specifically, linear transformations are used in geometry processing to encode complex nonrigid isometric maps between shapes [11]. Similarly, spectral approaches are utilized on fluid dynamics data to analyze the underlying system [36]. Motivated by these empirical examples and their success, we opt for a linearization of F .

Our method for computing C is general and it is potentially applicable to any time series $\{x_t\}$. However, the following two key assumptions are important for producing a meaningful C matrix. 1. Given an input sequence $\{x_t\}$ we can extract its associated state sequence $\{h_t\}$ directly from F . 2. After model (1) is trained, the hidden states $\{h_t\}$ lie next or on a *flat*¹ low-dimensional manifold for most or all input sequences. As computational models typically allow inspection, the first assumption is reasonable in a common setup. Furthermore, the second requirement is central in the manifold learning field [37, 38] with observations that carry over to other fields including deep learning. In particular, the results in [4] and other works show that $\{h_t\}$ are indeed low-dimensional for several models, tasks, and architectures.

Given a collection of hidden state sequences $\{h_{s,t}\}$, where s denotes a sequence index and t represents discrete time, we compute the matrix C by implementing two simple steps: 1. Represent the states using a *multiscale* basis B , and denote the resulting collection of spectral coefficients by $\{\tilde{h}_{s,t}\}$. That is, similar to Fourier analysis, we choose a basis that allows for an *ordered low dimensional* encoding of the data. 2. Find the best linear transformation C which maps $\tilde{h}_{s,t}$ to $\tilde{h}_{s,t+1}$ in the spectral domain, for every admissible s and t . We emphasize that an order of the basis elements is important as it facilitates our later analysis of the dominant modes in the dynamics. Nevertheless, it is not mandatory, i.e., we can employ other dimensionality reduction techniques which are not necessarily multiscale (i.e., ordered) such as autoencoders [39].

To give a specific example for the general procedure we described above, we can choose the principal components $b_j, j = 1, 2, \dots$ of the truncated SVD to be the basis in the first step. Then, the resulting basis elements are orthonormal, i.e., $\langle b_i, b_j \rangle = \delta_{ij}$, where δ_{ij} is the Kronecker delta. Computing the spectral coefficients $\tilde{h}_{s,t}$ is achieved via the projection

$$\tilde{h}_{s,t}(j) = \langle h_{s,t}, b_j \rangle, \quad (2)$$

where b_j is the j -th component. Then, we can compute C by solving the following least squares minimization

$$C := \arg \min_{\tilde{C}} \sum_{s,t} |\tilde{C}\tilde{h}_{s,t} - \tilde{h}_{s,t+1}|_2^2. \quad (3)$$

We note that the above scheme is a variant of the dynamic mode decomposition [40] and the functional maps [11] algorithms. A pseudocode for the latter example is provided in Alg. 1.

4 Results

4.1 The copy task

The copy task was designed to test the memory retaining capabilities of recurrent units [32]. In this task, the network is expected to memorize the first few characters in the input array and copy them to the end of the output vector which is otherwise filled with blanks. Thus, the challenge increases as the amount of blanks is higher. In what follows, we will show that RENN [5] essentially fails on this task, whereas our method achieves meaningful results.

¹We elaborate on this aspect in App. A.

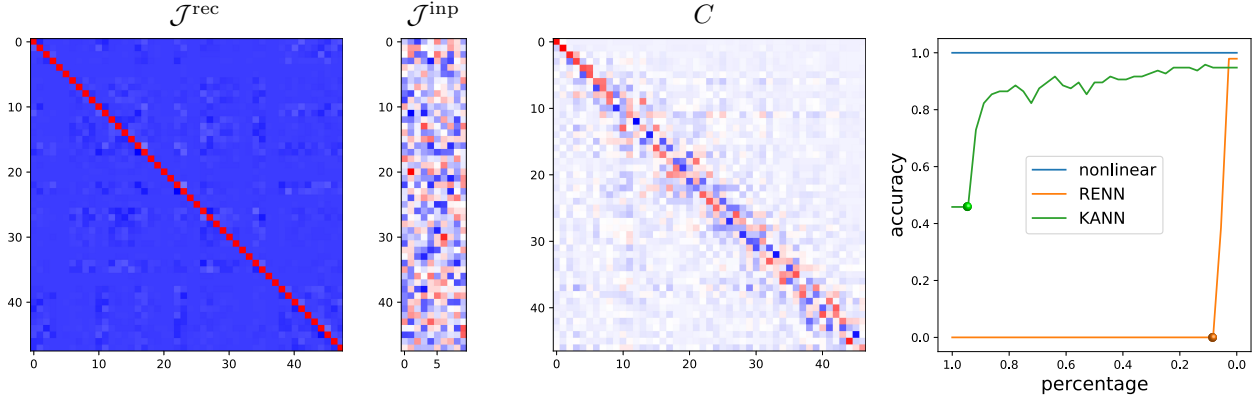


Figure 1: Computing RENN components for the copy task leads to an almost identity recurrent Jacobian, $|\mathcal{J}^{\text{rec}} - \text{id}| = 0.11$ relative error. In comparison, our matrix C is approximately orthogonal and it exhibits a diagonally-dominant structure. Consequently, RENN produces poor accuracy results with linearized paths, whereas our KANN approach attains significantly better measures. See the text.

We trained a `dtriv` architecture [41] on the copy task with three characters to remember and 30 blanks for 500 iterations. The network converges to an accuracy of 100% on the training and testing data as it is a relatively easy setting. The following analysis is based on a test batch of size 32, yielding a states tensor $H \in \mathbb{R}^{32 \times 37 \times 48}$ where the middle dimension is the sequence length including the initial state, and the last dimension is the hidden state size. We now discuss RENN results on this task, and then we show our analysis and observations.

We briefly recall that RENN uses H to generate a set of fixed points, i.e., points h^* for which the dynamical system in Eq. (1) is stationary $h^* \approx F(h^*, 0)$ [4]. Then, they derive their analysis using the input and recurrent Jacobians of F , \mathcal{J}^{inp} and \mathcal{J}^{rec} , evaluated at a single point $(h^*, x^* \equiv 0)$. We show in Fig. 1 the resulting Jacobian matrices using RENN where $\mathcal{J}^{\text{rec}} \approx \text{id}$ matrix (left). This is actually the expected result – as the blanks are mapped to zeros in this task, using $x^* \equiv 0$ means we look for fixed points h^* related to a blank input. However, the output for a blank input should be blank as well, and thus the hidden states converge to a section of the manifold which is indifferent to the inputs. To conclude, on the copy task, most of the nontrivial information of RENN is encoded in the input Jacobian, \mathcal{J}^{inp} . We note that it is not clear how to avoid this issue without using significant knowledge of the copy task during the computation of fixed points.

In comparison to \mathcal{J}^{rec} , our C matrix has a rich structure as can be seen in Fig. 1 (middle). There is a relatively simple interpretation for C . Namely, C pushes forward the hidden states in their *spectral* representation as given by the SVD modes. Thus, a diagonally-dominant matrix corresponds to (mostly) individual scalings of the different modes. That is, to faithfully describe the dynamical trajectory of the hidden states, it is sufficient to encode the growth and decay of the associated SVD modes. Moreover, the algebraic structure of the matrix is strongly related to the geometric features of the dynamics. Specifically, the matrix C is approximately orthogonal for the copy task, i.e., $C^T C \approx \text{id}$, and it is well-known that measure preserving maps correspond to unitary Koopman operators [42, 43]. Indeed, the copy task is measure preserving by definition, and thus our findings highlight that `dtriv` respects the structure of the problem. We state the result below, and we prove it in App. B for completeness.

Proposition 1 *Let φ be an invertible measure preserving dynamical system on a domain \mathcal{M} . Then its associated Koopman operator is unitary.*

To determine the affect of the structural difference between \mathcal{J}^{rec} and C we perform the following experiment. We use the RENN approach [5] and ours to linearize the hidden states path. In particular, we generate the linearized state h_{t+1}^{RENN} by employing

$$h_{t+1}^{\text{RENN}} := h^* + \mathcal{J}^{\text{rec}}(\bar{h}_t - h^*) + \mathcal{J}^{\text{inp}}x_t \quad (4)$$

$$\approx \bar{h}_t + \mathcal{J}^{\text{inp}}x_t, \quad (5)$$

where \bar{h}_t can be the original h_t or h_t^{RENN} , and the bottom formula is relevant when $\mathcal{J}^{\text{rec}} \approx \text{id}$ matrix. Fig. 1 shows the accuracy values as obtained from paths which are linearized across several thresholds (right). For instance, when the percentage is 30%, we use $\bar{h}_t = h_t$ for 70 percent of the path and then we take $\bar{h}_t = h_t^{\text{RENN}}$. Due to the trivial nature of \mathcal{J}^{rec} , RENN achieves zero accuracy in most cases, and it significantly improves when the last three states become

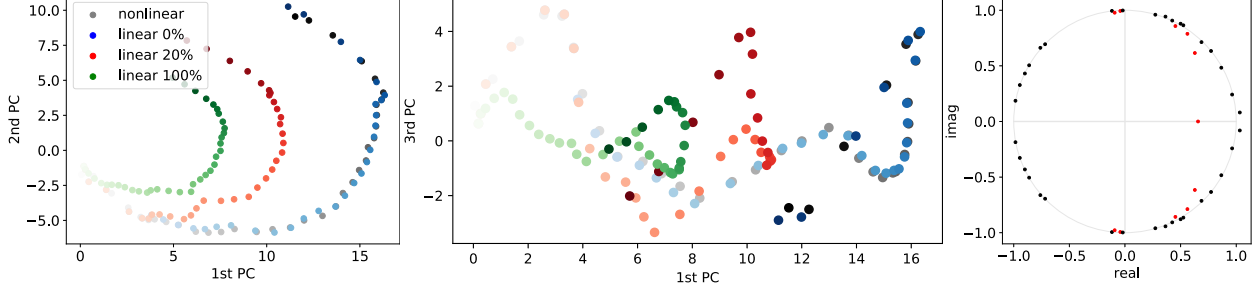


Figure 2: Our linearized paths exhibit a similar curved behavior as the nonlinear path when projected to the most dominant modes (left, middle). However, we also observe a shrinkage that increases with the level of linearity which can be explained by the appearance of decay modes in the spectrum of C (right). See the text.

available (marked by the orange point). Thus, RENN requires almost the entire sequence of ground-truth hidden states to produce good accuracy measures in this scenario.

We compute our linearized paths by repeatedly applying the matrix C on vectors that depend on the linear threshold percentage. Specifically, the linear hidden state h_{t+1}^{KANN} is defined via

$$h_{t+1}^{\text{KANN}} := B \cdot C \cdot B^T \bar{h}_t, \quad (6)$$

where B is the matrix of SVD modes in columns, and \bar{h}_t is either h_t or h_t^{KANN} based on the percentage threshold. We note that Eq. (6) is applicable only for a basis B which is linear and orthogonal. If these requirements are not met, a different formulation is needed. The accuracy results of KANN are extremely good (Fig. 1, green line), even when the percentage is high, i.e., most of the path does *not* use the states provided by the network. Further, we emphasize that the green point marks the percentage for three hidden states. That is, our method gets more than 80% accuracy exactly when all the non-blank input digits are implicitly available in the states. Therefore, our results highlight that C truly mimics the nonlinear dynamics as it is the minimal set of necessary inputs for a meaningful prediction.

In addition to comparing the accuracy measurements of the different linearized state paths, we also visualize their low-dimensional embeddings. Fig. 2 shows the paths obtained with our method when projected onto the first and second SVD modes (left) and first and third components (middle). We plot four different paths: the nonlinear states obtained from Eq. (1) (Greys), and the linear paths for thresholds 0% (Blues), 20% (Reds), and 100% (Greens). It is evident that increasing the linearity level of the path leads to a more significant shrinkage. We attribute these effects to eigenvectors of C whose eigenvalues are inside the unit circle. Indeed, the theory of dynamical systems analyzes the growth and decay of paths via the eigenvalues of the linearized system [3]. Fig. 2 (right) shows a few eigenvalues of C in the complex plane which we mark in red, that correspond to decaying modes.

Interestingly, the geometric structure of the paths is maintained. Namely, we obtain shrunk half-circles (Fig. 2, left) and similarly-curved paths (Fig. 2, middle). We note that the shrinkage is similar for the 1st and 2nd components, and it is less pronounced for the 3rd coordinate. This can be explained based on the variance of the different terms: 33%, 24%, and 4% for the 1st, 2nd, and 3rd SVD vectors, respectively. Overall, we believe this result is promising as it shows an approximate preservation of structure in latent spaces through the linearized dynamics we capture with C . We believe it can be further used to improve the training of nonlinear neural networks and to design equivariant computational sequence models. We leave further analysis and investigation of this direction to future work.

4.2 Sentiment Analysis

Determining the sentiment of a document is an important problem which may be viewed as a binary classification task [44]. We will use the IMDB reviews dataset [45], where the role of the network is to output whether a given review is positive or negative. This task was extensively studied in [5]. We adopt their network structure which uses word embeddings of size 128, and a GRU recurrent layer with a hidden size of 256. One of the main results using RENN [5] was the observation that the dynamics of the network spans a line attractor. That is, the hidden states of the network are positioned on a one dimensional manifold, splitting the domain into positive and negative sentiments.

The low dimensional structure of the problem facilitates the study of the features of our matrix C . Specifically, we will show that it is sufficient to track the temporal coefficients of merely three SVD modes to understand the dynamics. Namely, to a large extent, a 3×3 matrix C can replace the system F . Moreover, in our representation, the dominant SVD vector is an approximate fixed point, i.e., $b_1 \mapsto_F b_1$, and thus the sign of the spectral coefficients is instrumental

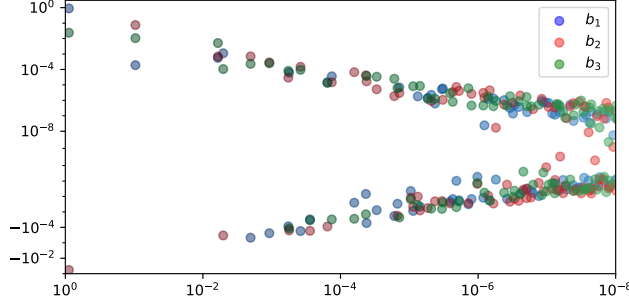


Figure 3: We plot the scaled spectral coefficients of $C\tilde{b}_j$ for each variance item in the SVD for the dominant three modes. Due to the low values of most terms, the behavior of the system can be determined by the first three components. See the text.

during classification. Finally, inference of the sentiment is realized by summing the weighted three coordinates of the last state. Our results are aligned with those of RENN, and we offer additional interpretations of the system.

We train the model for 5 epochs during which it reaches an accuracy of $\approx 92\%$, 87% , 87% on the train, validation and test sets, respectively. For analysis, we extract a random test batch of 64 reviews and its states $H \in \mathbb{R}^{64 \times 1001 \times 256}$, where 1000 is the sequence length when padded with zeros. We take the truncated SVD [46] components to be our basis B . In this case, the explained variance ratio of the three dominant modes is $[86.9\%, 10\%, 2.5\%]$. That is, three vectors encode $> 99\%$ of the variability in the hidden states tensor. The test batch attains 91% accuracy, and we additionally compare the accuracy for varying degrees of linearity for our method and RENN, see Tab 1. Overall, the methods perform similarly, except for high degrees of linearity. This can be explained by recalling that RENN can access the inputs $x_t, \forall t$, per Eq. (4). In contrast, our method uses the inputs only up to the linearity threshold. Thus, for dominantly linear paths, we exploit less information which naturally reduces the accuracy measures.

Linearity	0%	20%	40%	60%	80%	90%
RENN	91%	91%	91%	92%	84%	89%
KANN	91%	91%	91%	92%	84%	76%

Table 1: Similarly to Fig. 2 (right), we compare the accuracy of linearized paths over various degrees of linearity per Eq. (4) and Eq. (6) for RENN and KANN, respectively.

To further analyze the latent dynamics using the evolution matrix C , we consider the following visualization. Denote the spectral coefficients of the dominant three basis items by $\tilde{b}_j, j = 1, 2, 3$. Then, we would like to explore how these modes change due to the dynamics. Importantly, the basis elements can be considered as hidden states, and thus we can directly multiply \tilde{b}_j by C to determine their paths. We plot the resulting spectral coefficients for b_1 (blue), b_2 (red), and b_3 (green) in Fig. 3. The coefficients are scaled by their respective variance, e.g., the coordinates of the first component are multiplied by 0.87, and so on. The logarithmic scale on both axes emphasizes that most values are in $[-10^{-4}, 10^{-4}]$, yielding a negligent effect to the dynamics.

$\langle C\tilde{b}_i, \tilde{b}_j \rangle$	$j = 1$	$j = 2$	$j = 3$
$i = 1$	1.005	0.002	0.09
$i = 2$	-0.065	0.784	0.113
$i = 3$	0.027	0.11	0.846

Table 2: The non-scaled coordinates $\langle C\tilde{b}_i, \tilde{b}_j \rangle$ for $i, j = 1, 2, 3$.

We further provide in Tab. 2 the non-scaled matrix values of the dominant modes. The basis vectors are approximate fixed points of the dynamics since the main diagonal values are close to one, and are otherwise zero. Specifically, the vector b_1 satisfies $C\tilde{b}_1 = \tilde{b}_1 + \mathcal{O}(1e-3)$. Our observation is instrumental to determine the sentiment of a review as

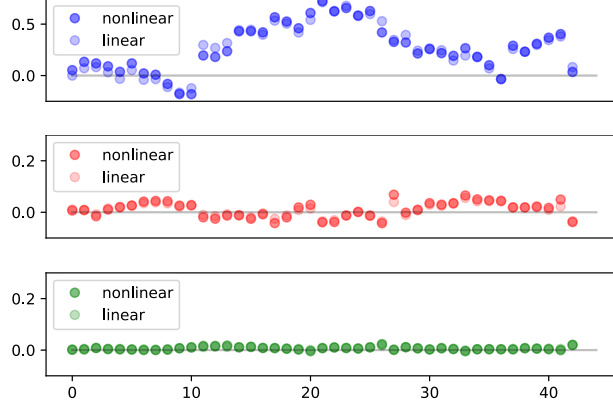


Figure 4: Visualizing the weighted spectral coefficients for the first, second, and third components (top, middle, and bottom) over time highlights the importance of the last hidden state and its sign.

we discuss now. We expand Eq. (6) in the spectral domain to analyze the i -th element of the next hidden state, i.e.,

$$\begin{aligned}\tilde{h}_{t+1}(i) &= [B^T h_{t+1}](i) \\ &\approx [C \tilde{h}_t](i) = \sum_j C(i, j) \tilde{h}_t(j).\end{aligned}\quad (7)$$

For instance, if $i = 1$ then $\tilde{h}_{t+1}(1) \approx \tilde{h}_t(1)$ since $C(i, j)$ is almost zero for all $j > 1$, and $C(1, 1) \approx 1$. Thus, in a binary classification setting such as ours, the sign of $\tilde{h}_t(1)$ will largely determine the output sentiment.

Using our framework and the observations above, we aim at inferring the sentiment per review. Let us denote the true label for a single review s of the input sequence $\{x_{s,t}\}$ by $\hat{y}_s \in \{0, 1\}$. Similarly, we use y_s for the label predicted by the network, i.e., $y_s = G(h_{s,T})$ where G is some nonlinear neural function, and T is the index of the last hidden state. We note that in sentiment analysis models, only the last hidden state is typically used for inference. We propose to compute y_s^{KANN} of $h_{s,T}$ such that $y_s^{\text{KANN}} = y_s$ for all s . To this end, we take the sign of the weighted coefficients sum, scaled to the range zero to one. Formally,

$$y_s^{\text{KANN}} = \frac{1}{2} \text{sign} \left(\sum_{j=1}^3 p(j) \cdot \tilde{h}_{s,T}(j) \right) + \frac{1}{2}, \quad (8)$$

where $\text{sign}(\cdot)$ is the sign function, $p \in \mathbb{R}_+^3$ is the explained variance for the three dominant components, and $\tilde{h}_{s,T}$ is the spectral coefficients vector of the last hidden state $h_{s,T}$.

For example, we extract a single review from the test set with 44 tokens. The first spectral coordinates are given by $\tilde{h}_T = [0.077, -0.176, 0.568]$, and $p = [0.869, 0.1, 0.025]$, yielding the label $y_s^{\text{KANN}} = 1$ which is equal to y_s and \hat{y}_s . For reference, we also plot the weighted coefficients over time for this review in Fig. 4. The top, middle and bottom graphs correspond to the first, second, and third truncated SVD vectors. The dark and light color schemes represent the nonlinear and 0% linear paths, respectively. In addition, we evaluate Eq. (8) on 250 batches from the test set. The labels y_s^{KANN} we compute match y_s on 98% of the 16,000 samples. This result is particularly impressive given that we use only three basis elements. Interestingly, the average accuracy of the new labels exceeds the average accuracy of the network outputs, 86.84% vs. 86.28%. Finally, the per batch error histogram reads: $[70, 89, 53, 31, 6, 1]$ batches attain $[0, 1, 2, 3, 4, 5]$ errors across the batch, respectively.

4.3 ECG Classification

Electrocardiogram (ECG) tests track the electrical activity in the heart, and they help detect various abnormalities in a non-invasive way. In particular, classifying whether a beat is normal or not is a challenging task [47] which lacks descriptive neural models. To this end, we will focus on a common architecture for ECG classification that is based on LSTM autoencoders [48]. Our network is composed of a single layer LSTM encoder with a hidden size of 64, and an LSTM decoder with one layer as well. We use a publicly available subset of the MIT-BIH arrhythmia database [49]

for our data, named ECG5000². This dataset includes 5000 sample heartbeats with a sequence length of 140. Around 60% of the sequences are classified as normal and the rest are various anomalous signals.

While we consider the current task as a binary classification problem, there are several important differences between detecting anomalies in ECG signals and the SA problem we study in Sec. 4.2. In particular, the sentiment of a review is the direct outcome of the network, whereas for ECG, we make a decision based on the loss of the reconstructed signal when passed through the autoencoder. Therefore, the high dimensional generative nature of the model makes it more prone to small errors in the network. Further, the latent structure of the neural network post training is high dimensional in comparison to SA where it is essentially 1D. Specifically, we use a test batch of 20 beats and its hidden states tensor $H \in \mathbb{R}^{20 \times 141 \times 64}$, represented in the truncated SVD basis. In this setting, the explained variance ratios our model yields for the five dominant components read:

$$18.3\%, 13.6\%, 10.1\%, 8.4\%, 7.9\% ,$$

i.e., these modes explain only 58.6% of the variance, and one needs at least 17 vectors to span $> 90\%$ of the variance.

Given the above differences, we expect that understanding and analyzing recurrent models for ECG classification may be more challenging compared to the SA setting. To deal with these difficulties we will show that there is a more “natural” basis for C than the basis used for the states. The new basis V is formed from the eigenvectors of C , and it is complex-valued, unless the operator is symmetric. Further, V shares some of the fundamental aspects of the truncated SVD modes. Namely, every latent state can be represented with this basis via linear projection, similarly to Eq. (2). Furthermore, the basis elements can be ordered and sorted with respect to their dynamical dominance. Finally and in contrast to the SVD basis, it is guaranteed that the Koopman operator represented in the V basis is always *diagonal*, and thus easy to process and analyze.

The latter observations can be derived in the following way. Given an approximate Koopman operator C , consider its eigenvalues $\lambda_j \in \mathbb{C}$ and eigenvectors $v_j \in \mathbb{C}^k$, i.e., it holds that $C v_j = \lambda_j v_j$. Let $h_{s,t}$ be some state and denote by $\hat{h}_{s,t}$ its spectral coefficients in the basis $V = (v_j)$. That is, analogously to Eq. (2) we have,

$$\hat{h}_{s,t} = V^{-1} B^T h_{s,t} . \quad (9)$$

Then, re-writing Eq. (6) using the eigendecomposition of C allows to formulate the temporal trajectory of $h_{s,t}$ via

$$\begin{aligned} \hat{h}_{s,t+1} &= V^{-1} B^T h_{s,t+1} \\ &\approx V^{-1} C B^T h_{s,t} = \Lambda V^{-1} B^T h_{s,t} \\ &= \Lambda \hat{h}_{s,t} = \left(\lambda_j \cdot \hat{h}_{s,t}(j) \right) , \end{aligned} \quad (10)$$

where Λ is the diagonal matrix of eigenvalues, and the approximation is due to Eq. (6). Consequently, we obtain that $h_{s,t+1} \approx \sum_j \hat{h}_{s,t}(j) \lambda_j v_j$.

Based on the derivation (10) and its corollary, we can see that the (linearized) dynamics using V are fully separable. Indeed, each eigenvector is propagated independently of the other vectors, and it is scaled by the eigenvalue and $\hat{h}_{s,t}$. Thus, represented in the eigenvectors basis, the linear dynamics matrix is simply Λ . Further, it directly follows that $\hat{h}_{s,t+k} \approx \left(\lambda_j^k \cdot \hat{h}_{s,t}(j) \right)$, that is, the number of steps forward is determined by the eigenvalue’s power. Finally, the basis elements can be naturally sorted using the norm of λ_j . We refer the reader to [36, 50] for a more comprehensive discussion on this topic.

We asses the importance of eigenvectors in the analysis of ECG classification in the following way. First, the LSTM autoencoder is trained for 150 epochs, yielding an accuracy of 98.5%, 98.9%, 97.9% on the train, validation and test sets, respectively. Then, we extract a test batch of *normal* beats and its states tensor H . Next, we compute the matrix C and its eigendecomposition, storing the eigenvalues in a matrix Λ , and the eigenvectors in V . Every vector in V could be viewed as a hidden state, and thus we can compute its linear trajectory as governed by C . Based on the results above, the paths take the following form

$$v_{j,k} = \lambda_j^k v_{j,0} , \quad (11)$$

i.e., the j th eigenvector at time zero, $v_{j,0}$, is pushed to the k th time step by multiplying the vector by the k th power of the related eigenvalue. We denote by $f_{j,k}$ the reconstructed beat from the real part of $v_{j,k}$ for every $k \in \{1, \dots, 140\}$. The value 140 was chosen as it represents a single full cycle for the beat signals.

²<http://timeseriesclassification.com/description.php?Dataset=ECG5000>

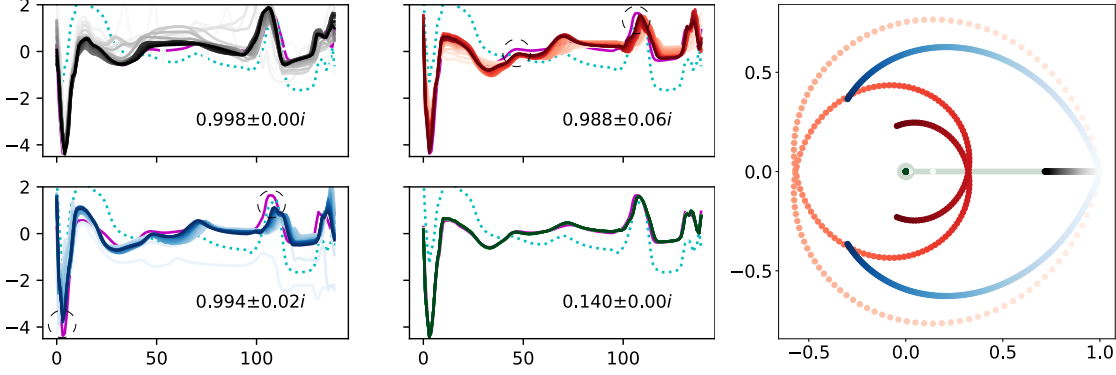


Figure 5: We show the network reconstructions for the most dominant modes (Greys, Blues, Reds) and the least significant eigenvector (Greens). We also plot the beats corresponding to the zero state (magenta) and dominant SVD mode (dotted cyan). In addition, we employ the same color schemes for the associated eigenvalues’ paths, showing two trajectories for complex-valued λ_j . See the text.

Fig. 5 shows the reconstructed beats over time, where we focus on the three most significant vectors and the least dominant mode based on their eigenvalue norm. We use a sequential colormap for each path collection $\{v_{j,k}\}_{k=0}^{140}$ with Greys, Blues, Reds, and Greens for modes with eigenvalues 0.998 , $0.994 \pm 0.016i$, $0.988 \pm 0.057i$, and 0.14 , respectively. In practice, the eigenvectors converge within $k < 20$ iterations to a representative beat which is propagated forward in time until the eigenvalue vanishes. Further, we plot the reconstructed beats for the zero state in magenta, and the most dominant SVD mode in dotted cyan. Finally, we show in the right of Fig. 5 the paths of the respective eigenvalues and their powers for every k , using the same color schemes we used for the beats. Noticeably, the green trajectory (0.14) quickly converges to zero, whereas the paths of the dominant modes remain, even after 140 applications of the matrix C .

The first observation we make regarding the above results is that the eigenvectors V are “aware” of the dynamics in comparison to the SVD modes. Indeed, each of the eigenvectors can be viewed as an approximate fixed point of the dynamics F in Eq. (1) as we have $v_{j,k+1} \approx C v_{j,k}$, for all j and for moderate k . Moreover, the eigenvectors converge to the beat signal of the zero state (Greys, Greens), or diverge from it slightly (Blues, Reds). In comparison, the SVD mode’s beat in dotted cyan is not close to any of those signals. This is somewhat expected as the SVD modes mostly encode the variability in the data, and thus may be viewed as the average normal signal per test batch. In this context, we can interpret the eigenvectors as the modes which are important to the decision and inference processes of the neural model. Importantly, most of the vectors v_j are associated with extremely small deviations from the zero state, and thus they do not contribute much to the dynamics. In practice, the long-term behavior of the network is governed by the signals plotted in Fig. 5.

Our second key finding is related to the model encoding of *normal* vs. *anomalous* beats. Viewed in the eigenvalues complex plane, we find that the model develops a “needle”-like robust region along the values $[0, 1]$. Namely, all the reconstructed beats along the path from 1 to 0, and in the neighborhood of zero are similar and classified as normal beats. In contrast, the other dominant modes (Blues and Reds) capture deviations from the limit beat as marked by the dashed circles over the missed peaks. These vectors are instrumental to the model detection of anomalies since anomalous beats are mostly described by the blue and red vectors via projection (9). We conclude that the network distinguishes between signals by measuring their deviation from the network’s encoding of the limit beat.

5 Discussion

In this work we presented a novel framework for studying sequence neural models based on Koopman Theory. Our method involves a dimensionality reduction representation of the states, and the computation of a linear map between the current state and the next state. Key to our approach is the wealth of tools we can exploit from linear analysis and Koopman-related work. In particular, we compute linear approximations of the state paths via simple matrix-vector multiplications. Moreover, we identify dominant features of the dynamical system and their affect on inference and prediction. Our results on the copy task, and sentiment and ECG classification provide simple yet accurate descriptions of the underlying dynamics and behavior of the recurrent models. We believe that our work will encourage others to develop techniques towards understanding neural networks better. In the future, we will explore the relation between the curved structure of state paths and the training process.

References

- [1] Kenji Doya. Bifurcations of recurrent neural networks in gradient descent learning. *IEEE Transactions on neural networks*, 1(75):218, 1993.
- [2] Razvan Pascanu, Tomas Mikolov, and Yoshua Bengio. On the difficulty of training recurrent neural networks. In *ICML*, pages 1310–1318, 2013.
- [3] Steven H Strogatz. *Nonlinear dynamics and chaos: With applications to physics, biology, chemistry, and engineering*. CRC press, 2018.
- [4] David Sussillo and Omri Barak. Opening the black box: low-dimensional dynamics in high-dimensional recurrent neural networks. *Neural computation*, 25(3):626–649, 2013.
- [5] Niru Maheswaranathan, Alex Williams, Matthew Golub, Surya Ganguli, and David Sussillo. Reverse engineering recurrent networks for sentiment classification reveals line attractor dynamics. In *NeurIPS*, pages 15696–15705, 2019.
- [6] Kyle Aitken, Vinay V Ramasesh, Ankush Garg, Yuan Cao, David Sussillo, and Niru Maheswaranathan. The geometry of integration in text classification RNNs. *arXiv preprint arXiv:2010.15114*, 2020.
- [7] Bernard O Koopman. Hamiltonian systems and transformation in Hilbert space. *Proceedings of the national academy of sciences of the united states of america*, 17(5):315, 1931.
- [8] Omri Azencot, N. Benjamin Erichson, Vanessa Lin, and Michael W. Mahoney. Forecasting sequential data using consistent Koopman autoencoders. In *ICML*, volume 119, pages 475–485, 2020.
- [9] Igor Mezić. Spectral properties of dynamical systems, model reduction and decompositions. *Nonlinear Dynamics*, 41(1-3):309–325, 2005.
- [10] Abhishek Sharma and Maks Ovsjanikov. Weakly supervised deep functional maps for shape matching. In *NeurIPS*, 2020.
- [11] Maks Ovsjanikov, Mirela Ben-Chen, Justin Solomon, Adrian Butscher, and Leonidas Guibas. Functional maps: a flexible representation of maps between shapes. *ACM Transactions on Graphics (TOG)*, 31(4):1–11, 2012.
- [12] Kenji Doya. Universality of fully connected recurrent neural networks. *Dept. of Biology, UCSD, Tech. Rep.*, 1993.
- [13] Yoshua Bengio, Paolo Frasconi, and Patrice Simard. The problem of learning long-term dependencies in recurrent networks. In *IEEE international conference on neural networks*, pages 1183–1188. IEEE, 1993.
- [14] Thomas Laurent and James von Brecht. A recurrent neural network without chaos. In *ICLR*, 2017.
- [15] Bo Chang, Minmin Chen, Eldad Haber, and Ed H. Chi. AntisymmetricRNN: A dynamical system view on recurrent neural networks. In *ICLR*, 2019.
- [16] Martín Arjovsky, Amar Shah, and Yoshua Bengio. Unitary evolution recurrent neural networks. In *ICML*, volume 48, pages 1120–1128, 2016.
- [17] Mario Lezcano Casado and David Martínez-Rubio. Cheap orthogonal constraints in neural networks: A simple parametrization of the orthogonal and unitary group. In *ICML*, volume 97, pages 3794–3803, 2019.
- [18] Michiel Hermans and Benjamin Schrauwen. Training and analysing deep recurrent neural networks. *NeurIPS*, 26:190–198, 2013.
- [19] Andrej Karpathy, Justin Johnson, and Li Fei-Fei. Visualizing and understanding recurrent networks. *arXiv preprint arXiv:1506.02078*, 2015.
- [20] Edward Choi, Mohammad Taha Bahadori, Jimeng Sun, Joshua Kulas, Andy Schuetz, and Walter Stewart. Retain: An interpretable predictive model for healthcare using reverse time attention mechanism. *NeurIPS*, 29:3504–3512, 2016.
- [21] Scott M. Lundberg and Su-In Lee. A unified approach to interpreting model predictions. In *NeurIPS*, pages 4765–4774, 2017.
- [22] Sana Tonekaboni, Shalmali Joshi, Kieran Campbell, David Duvenaud, and Anna Goldenberg. What went wrong and when? instance-wise feature importance for time-series black-box models. In *NeurIPS*, 2020.
- [23] Naoya Takeishi, Yoshinobu Kawahara, and Takehisa Yairi. Learning Koopman invariant subspaces for dynamic mode decomposition. In *NeurIPS*, pages 1130–1140, 2017.
- [24] Jeremy Morton, Antony Jameson, Mykel J Kochenderfer, and Freddie Witherden. Deep dynamical modeling and control of unsteady fluid flows. In *NeurIPS*, pages 9258–9268, 2018.

- [25] Bethany Lusch, J Nathan Kutz, and Steven L Brunton. Deep learning for universal linear embeddings of nonlinear dynamics. *Nature communications*, 9(1):1–10, 2018.
- [26] N Benjamin Erichson, Michael Muehlebach, and Michael W Mahoney. Physics-informed autoencoders for lyapunov-stable fluid flow prediction. *arXiv preprint arXiv:1905.10866*, 2019.
- [27] Yunzhu Li, Hao He, Jiajun Wu, Dina Katabi, and Antonio Torralba. Learning compositional Koopman operators for model-based control. In *ICLR*, 2020.
- [28] Andreas Mardt, Luca Pasquali, Hao Wu, and Frank Noé. VAMPnets for deep learning of molecular kinetics. *Nature communications*, 9(1):1–11, 2018.
- [29] Akshunna S. Dogra and William T. Redman. Optimizing neural networks via koopman operator theory. In *NeurIPS*, 2020.
- [30] Iva Manojlović, Maria Fonoberova, Ryan Mohr, Aleksandr Andrejčuk, Zlatko Drmač, Yannis Kevrekidis, and Igor Mezić. Applications of Koopman mode analysis to neural networks. *arXiv preprint arXiv:2006.11765*, 2020.
- [31] Jeffrey L Elman. Finding structure in time. *Cognitive science*, 14(2):179–211, 1990.
- [32] Sepp Hochreiter and Jürgen Schmidhuber. Long short-term memory. *Neural computation*, 9(8):1735–1780, 1997.
- [33] Kyunghyun Cho, Bart van Merriënboer, Çaglar Gülçehre, Dzmitry Bahdanau, Fethi Bougares, Holger Schwenk, and Yoshua Bengio. Learning phrase representations using RNN encoder-decoder for statistical machine translation. In *EMNLP*, pages 1724–1734, 2014.
- [34] Herbert Jaeger. The “echo state” approach to analysing and training recurrent neural networks-with an erratum note. *Bonn, Germany: German National Research Center for Information Technology GMD Technical Report*, 148(34):13, 2001.
- [35] Kaiming He, Xiangyu Zhang, Shaoqing Ren, and Jian Sun. Deep residual learning for image recognition. In *CVPR*, pages 770–778, 2016.
- [36] Clarence W Rowley, Igor Mezić, Shervin Bagheri, Philipp Schlatter, and Dan S Henningson. Spectral analysis of nonlinear flows. *Journal of fluid mechanics*, 641(1):115–127, 2009.
- [37] Mikhail Belkin and Partha Niyogi. Laplacian eigenmaps for dimensionality reduction and data representation. *Neural computation*, 15(6):1373–1396, 2003.
- [38] Ronald R Coifman and Stéphane Lafon. Diffusion maps. *Applied and computational harmonic analysis*, 21(1):5–30, 2006.
- [39] Ian Goodfellow, Yoshua Bengio, Aaron Courville, and Yoshua Bengio. *Deep learning*. MIT press Cambridge, 2016.
- [40] Peter J Schmid. Dynamic mode decomposition of numerical and experimental data. *Journal of fluid mechanics*, 656:5–28, 2010.
- [41] Mario Lezcano Casado. Trivializations for gradient-based optimization on manifolds. In *NeurIPS*, pages 9154–9164, 2019.
- [42] Raif M Rustamov, Maks Ovsjanikov, Omri Azencot, Mirela Ben-Chen, Frédéric Chazal, and Leonidas Guibas. Map-based exploration of intrinsic shape differences and variability. *ACM Transactions on Graphics (TOG)*, 32(4):1–12, 2013.
- [43] Tanja Eisner, Bálint Farkas, Markus Haase, and Rainer Nagel. *Operator theoretic aspects of ergodic theory*, volume 272. Springer, 2015.
- [44] Lei Zhang, Shuai Wang, and Bing Liu. Deep learning for sentiment analysis: A survey. *Wiley Interdisciplinary Reviews: Data Mining and Knowledge Discovery*, 8(4):e1253, 2018.
- [45] Andrew Maas, Raymond E Daly, Peter T Pham, Dan Huang, Andrew Y Ng, and Christopher Potts. Learning word vectors for sentiment analysis. In *Proceedings of the 49th annual meeting of the association for computational linguistics: Human language technologies*, pages 142–150, 2011.
- [46] Nathan Halko, Per-Gunnar Martinsson, and Joel A Tropp. Finding structure with randomness: Probabilistic algorithms for constructing approximate matrix decompositions. *SIAM review*, 53(2):217–288, 2011.
- [47] Fei Zhu, Fei Ye, Yuchen Fu, Quan Liu, and Bairong Shen. Electrocardiogram generation with a bidirectional LSTM-CNN generative adversarial network. *Scientific reports*, 9(1):1–11, 2019.

- [48] Nitish Srivastava, Elman Mansimov, and Ruslan Salakhudinov. Unsupervised learning of video representations using LSTMs. In *ICML*, pages 843–852, 2015.
- [49] Ary L Goldberger, Luis AN Amaral, Leon Glass, Jeffrey M Hausdorff, Plamen Ch Ivanov, Roger G Mark, Joseph E Mietus, George B Moody, Chung-Kang Peng, and H Eugene Stanley. Physiobank, physiotoolkit, and physionet: components of a new research resource for complex physiologic signals. *circulation*, 101(23):e215–e220, 2000.
- [50] Jonathan H Tu, Clarence W Rowley, Dirk M Luchtenburg, Steven L Brunton, and J Nathan Kutz. On dynamic mode decomposition: Theory and applications. *arXiv preprint arXiv:1312.0041*, 2013.

A Koopman Theory

In this appendix we justify our approach from a theoretical standpoint that is based on Koopman Theory [7]. Let φ be a discrete-time continuous dynamical system on a finite-dimensional domain \mathcal{M} . Formally,

$$z_{k+1} = \varphi(z_k), \quad (12)$$

where $z_k \in \mathcal{M}$, and $k = 0, 1, 2, \dots$ is an integer index of the time. Then, φ induces a *linear* operator \mathcal{K}_φ which we call the Koopman operator, and it is given by

$$\mathcal{K}_\varphi f(z_k) = f(z_{k+1}), \quad (13)$$

where $f : \mathcal{M} \rightarrow \mathbb{R}$ is a scalar function in a bounded inner product function space \mathcal{F} . It can be shown that \mathcal{K}_φ fully encodes the dynamics φ and vice versa [43]. Importantly, while φ is a transformation from the domain to itself, $\mathcal{K}_\varphi : \mathcal{F} \rightarrow \mathcal{F}$ acts on the space of functions. From a practical point-of-view, these functions may be interpreted as observations of the system, such as velocity, sea level, temperature, or hidden states in our setup.

To justify our approach we consider the dynamics φ in this work to be the *task*. For example, we view the map that associates between the input and output vectors in the copy task as a dynamical system. Specifically, assume the model is required to remember three digits, then the input-output structure reads

$$928 \text{---} : \text{---} \mapsto_\varphi \text{---} \text{---} \text{---} 928$$

Thus, the hidden states may be considered as observations of the dynamics at various points in time. Our data-driven approach to learn φ based on its observations H via a linear operator C closely resembles the theoretical setting we outlined above. However, there is a fundamental difference – the Koopman operator \mathcal{K}_φ is typically infinite-dimensional, whereas C is naturally finite-dimensional. Thus, the matrix C is only an approximation of \mathcal{K}_φ in the general case.

Another important aspect of our computational pipeline is the assumption that the hidden states are embedded in a flat low-dimensional manifold. Indeed, if the underlying manifold would be high-dimensional or not flat, it would be difficult to capture the essential features of the system. In practice, the hidden state observations we investigate satisfy our requirements across several tasks, architectures and datasets.

B Unitary Koopman Operators

Proposition 1 *Let φ be an invertible measure preserving dynamical system on a domain \mathcal{M} . Then its associated Koopman operator is unitary.*

Proof. Let $\varphi : \mathcal{M} \rightarrow \mathcal{M}$ be a map on the compact, inner-product space \mathcal{M} . We denote by μ the continuous measure on \mathcal{M} , and its induced metric $\|z\|$. The map φ is measure preserving, i.e., $\mu(\varphi^{-1}A) = \mu(A)$ for every measurable set $A \subset \mathcal{M}$. Let \mathcal{K}_φ be the Koopman operator of φ acting on the function space of square integrable function L^2 . Given the indicator function 1_A for the set A , we have that

$$\mathcal{K}_\varphi 1_A(z) = 1_A(\varphi \circ z) = 1_{\varphi^{-1}A}(z),$$

and thus

$$\int_{\mathcal{M}} \mathcal{K}_\varphi 1_A d\mu = \mu(\varphi^{-1}A) = \mu(A) = \int_{\mathcal{M}} 1_A d\mu.$$

Moreover, positive functions converge to a representation using simple indicator functions. Consequently, we have that $\int_{\mathcal{M}} \mathcal{K}_\varphi f d\mu = \int_{\mathcal{M}} f d\mu$ for general $f \in L^2$ since it can be written as the difference of the integrable negative and positive components of f .

Table 3: The following hyperparameters per task and model were used during training.

Task	Architecture	#epochs	#units	Optimizer	LR	LR Scheduler	Clip
Copy Task	dtriv	500	48	RMSprop	1e-3	—	—1
Copy Task	RNN	10k	64	RMSprop	5e-3	ExpLR, $\gamma = 0.85$	5
Copy Task	GRU	285	48	RMSprop	1e-2	—	—1
Copy Task	LSTM	6.5k	48	RMSprop	5e-3	—	10
Sentiment Analysis	RNN	7	128	Adam	5e-3	ExpLR, $\gamma = 0.6$	15
Sentiment Analysis	GRU	5	256	Adam	5e-3	ExpLR, $\gamma = 0.5$	15
Sentiment Analysis	LSTM	5	256	Adam	1e-3	ExpLR, $\gamma = 0.3$	5
ECG Classification	GRU	150	64	Adam	1e-3	—	—1
ECG Classification	LSTM	150	64	Adam	1e-3	—	—1

The Koopman operator is linear and it is pointwise multiplicative, i.e., $\mathcal{K}_\varphi(\alpha f + \beta g) = \alpha \mathcal{K}_\varphi(f) + \beta \mathcal{K}_\varphi(g)$ and $\mathcal{K}_\varphi(fg) = \mathcal{K}_\varphi(f)\mathcal{K}_\varphi(g)$, where $\alpha, \beta \in \mathbb{R}$, and $f, g \in L^2$. Due to these observations, it follows that \mathcal{K}_φ preserves the inner product of functions, namely, for every $f, g \in L^2$

$$\langle f, g \rangle = \int_{\mathcal{M}} f g \, d\mu = \int_{\mathcal{M}} \mathcal{K}_\varphi(fg) \, d\mu = \langle \mathcal{K}_\varphi(f), \mathcal{K}_\varphi(g) \rangle.$$

Thus, the Koopman operator in this case is an isometry, since

$$d(f, g) = \|f - g\| = \langle f - g, f - g \rangle^{\frac{1}{2}} = \langle \mathcal{K}_\varphi(f - g), \mathcal{K}_\varphi(f - g) \rangle^{\frac{1}{2}}.$$

Finally, if φ is invertible then $\mathcal{K}_\varphi^* \mathcal{K}_\varphi = \mathcal{K}_\varphi \mathcal{K}_\varphi^*$ where \mathcal{K}_φ^* is the adjoint operator, and thus \mathcal{K}_φ is unitary.

C Additional Results

In this section, we provide additional results on the copy task, and sentiment analysis and ECG classification problems using different architectures. We focus on three common units which are used to construct most existing recurrent models. Namely, we employ vanilla recurrent neural networks (RNN) [31], gated recurrent units (GRU) [33], and long-short term memory units (LSTM) [32]. For every task and architecture, the results we present include the visualization of the operator C and its eigenvalue spectrum (Figs. 6, 7, 8). Moreover, we demonstrate the low-dimensional embedding of the linearized paths when projected to the first, second and third truncated SVD components on the copy task and ECG classification problem (Figs. 9, 10). We also extract a particular review from the IMDB dataset and plot its truncated SVD coefficients with respect to the RNN, LSTM, and GRU models in Fig. 11. Overall, most of our results are consistent with the observations we make in the main text, with some variations which can be attributed to a particular architecture or a specific problem. We briefly discuss the latter differences as well as explain them below.

In our experiments, we opt for an as basic as possible training procedure per task and model such that the obtained results yield comparable loss and accuracy measures. In most cases, we followed the standard training procedures which are commonly used on the selected tasks. We detail in Tab. 3 where architecture lists the specific unit we used, #units is the dimension of the hidden state, and LR is the initial learning rate. In several cases we employed a learning rate exponential scheduler (ExpLR) and gradient clipping (—1 is no clipping).

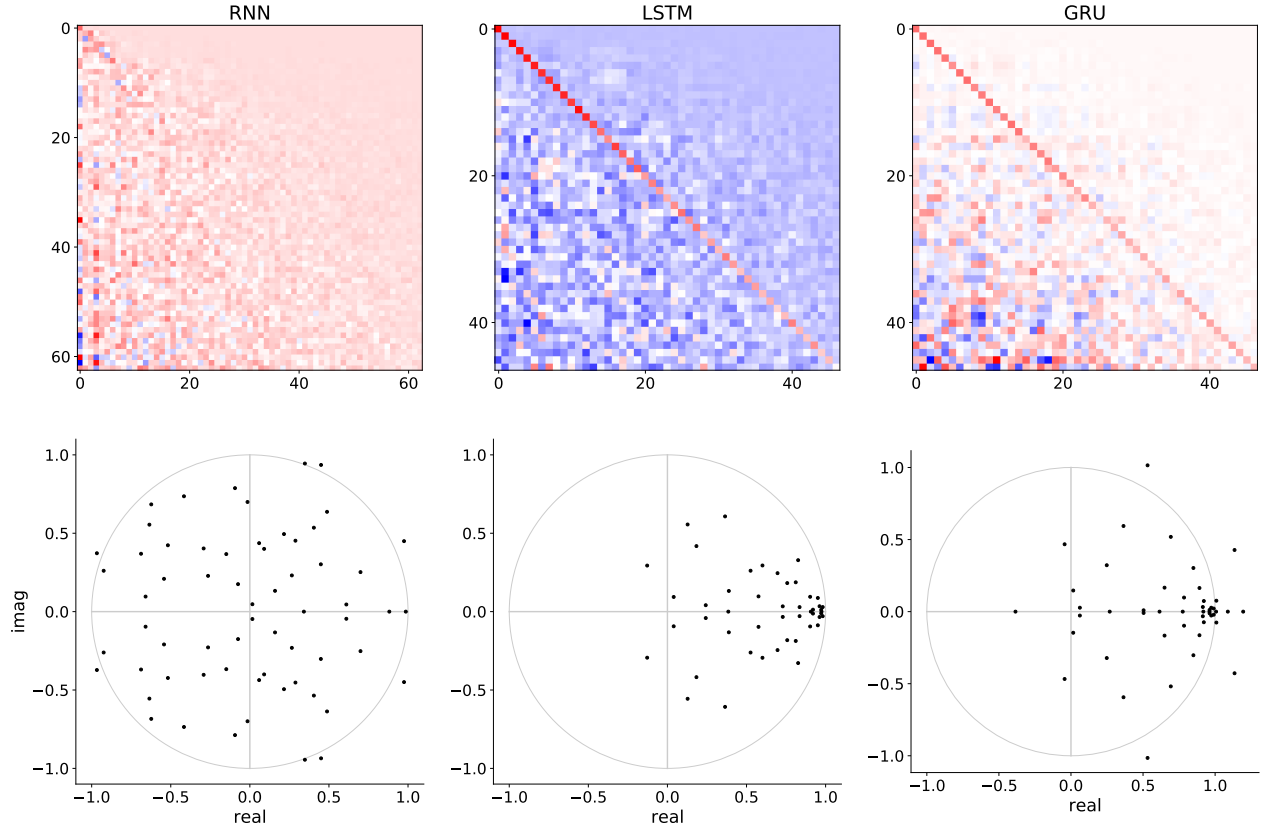


Figure 6: We show in the top row the various C matrices we obtain for the copy task using the RNN, LSTM and GRU units. For each matrix, we present its corresponding eigenvalue spectrum in the bottom row. Interestingly, while all units achieve $> 95\%$ accuracy results on this task, we units (RNN and GRU) are not stable as they include eigenvalues whose norm is greater than 1.

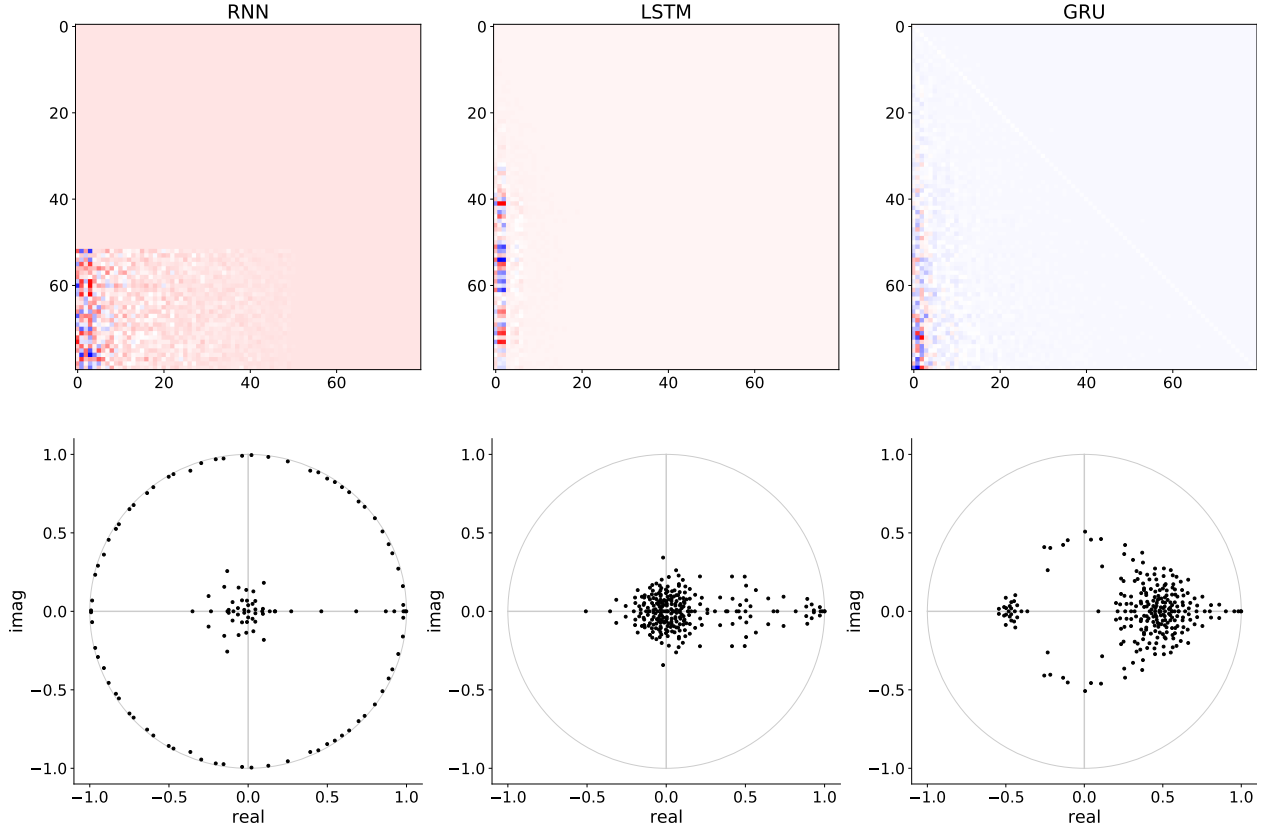


Figure 7: The sentiment analysis problem is unique in that three truncated SVD modes capture $\geq 95\%$ of the variability in the hidden states. Thus, the C matrices (top row) encode most of the information in the left part of the matrix. The spectra information for LSTM and GRU is similar with mostly decaying eigenvalues and a few unit norm modes. In contrast, RNN presents a completely different spectrum, where most of the eigenvalues are unit length.

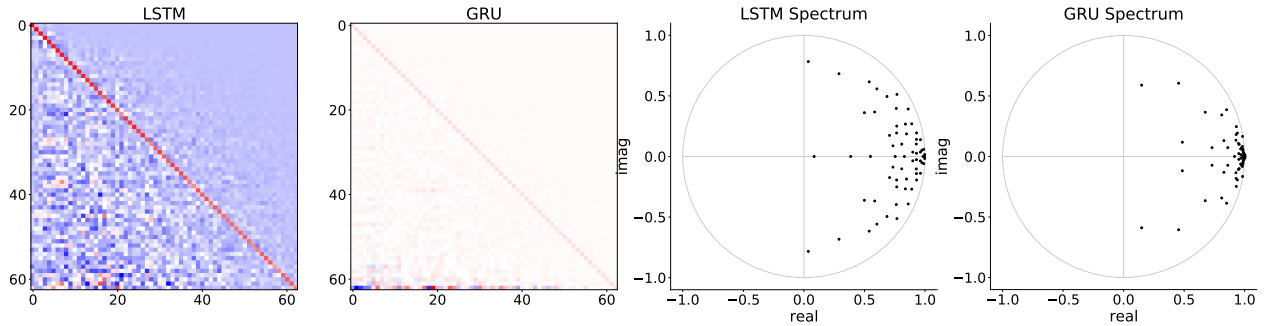


Figure 8: We show the C matrix and its spectrum for the LSTM and GRU units on the ECG classification task. In both cases, the matrices are similar in their structure and spectra.

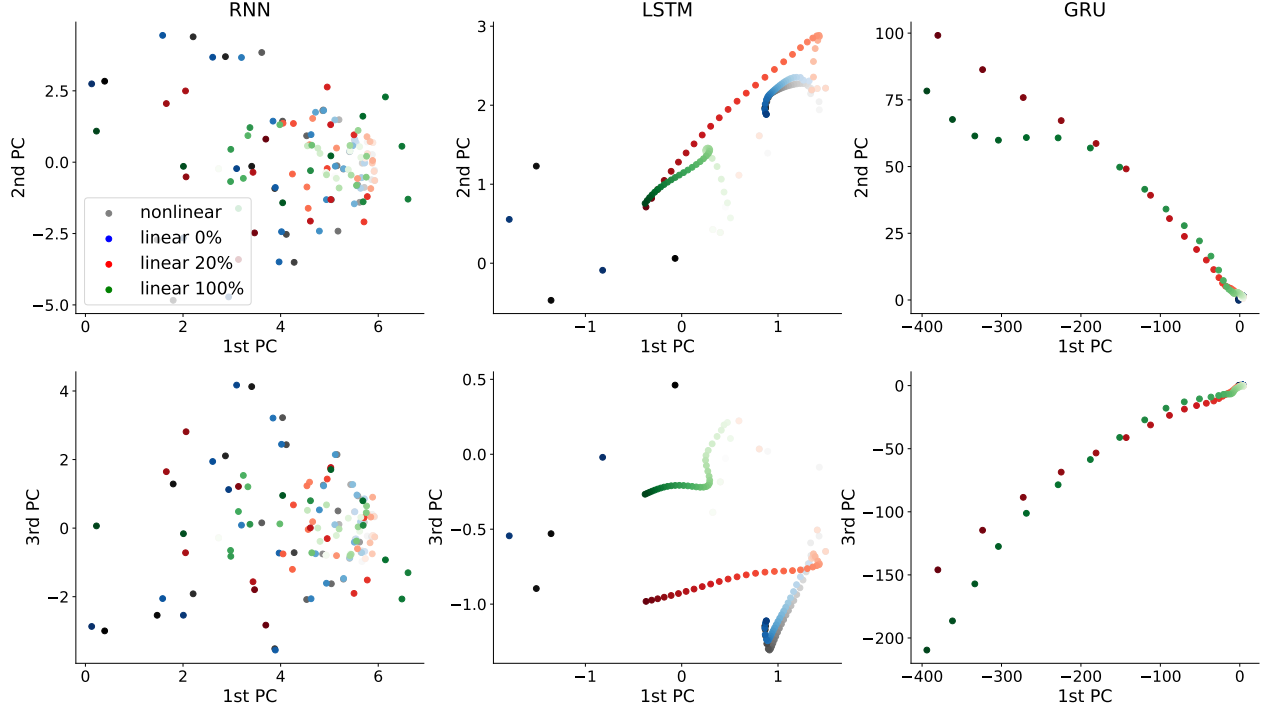


Figure 9: The coefficients of the first, second and third principal components are shown above in the context of the copy task. These coefficients correspond to various different paths: nonlinear (grey), 0% linear (blue), 20% linear, and 100% linear. See the main document for the definition of linearized paths. Evidently, the paths of the RNN unit are mixed with no clear structure, whereas LSTM and GRU generate paths with structural features, which are approximately maintained by our approach.

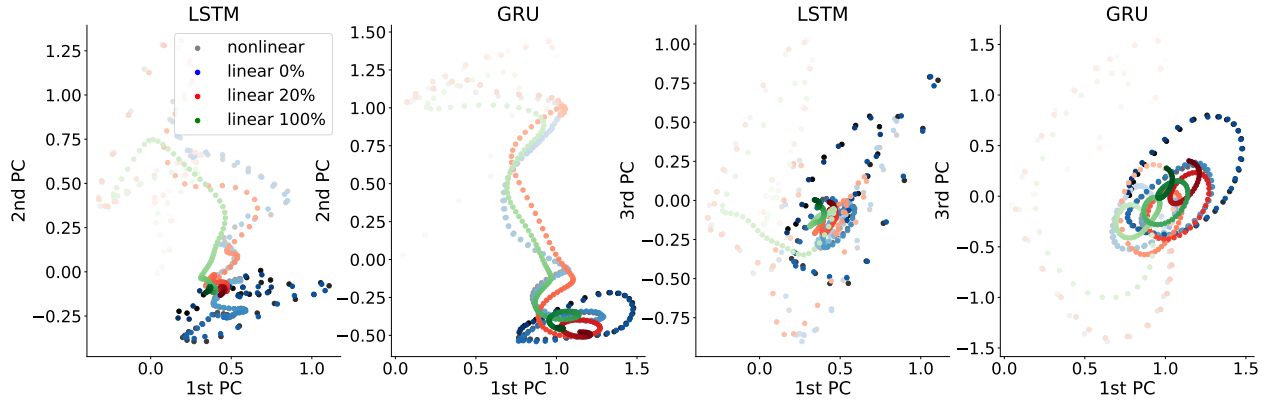


Figure 10: Similar to Fig. 9, we show the temporal principal component coefficients of LSTM and GRU on the ECG classification task. Here, again, both methods develop clear structures in the latent space, and our method approximately follows these structures.

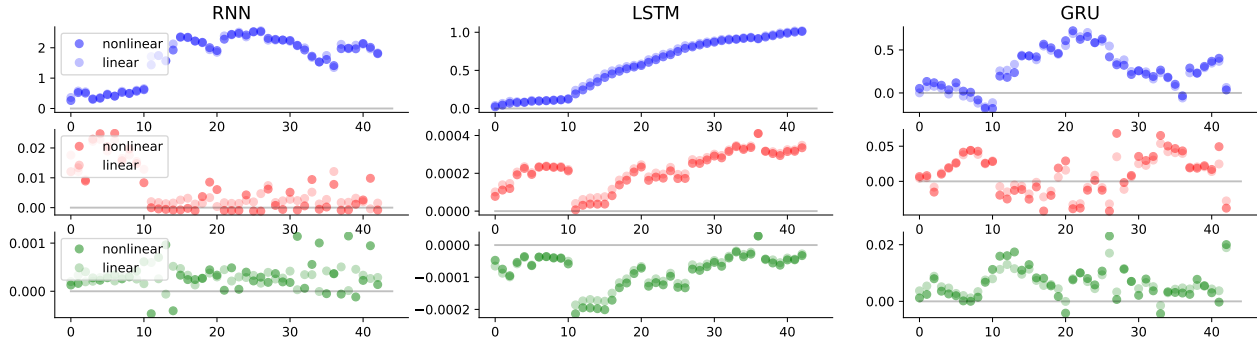


Figure 11: We show the spectral coefficients of a particular review in the sentiment analysis problem for various architectures. Our results highlight that the sign of the coefficients is instrumental to determine the sentiment of a review. In particular, in this example, the review’s true label is positive. If one inspects the coefficients of the last hidden state (i.e., at time T), it becomes evident that the nonlinear path as well as linear yield the same sentiment across all architectures.